



Weakly coordinating cationic polymer electrolytes for fast-charging solid-state lithium-metal batteries

Soohyoung Lee^{a,1}, Kyeong-Seok Oh^{b,1}, Ji Eun Lee^c, Sun-Phil Han^d, Hong-I Kim^b, Sang Kyu Kwak^{e,*}, Sang-Young Lee^{a,b,*}

^a Department of Battery Conflation Engineering, Yonsei University, 50 Yonsei-ro, Seodaemun-gu, Seoul 03722, Republic of Korea

^b Department of Chemical and Biomolecular Engineering, Yonsei University, 50 Yonsei-ro, Seodaemun-gu, Seoul 03722, Republic of Korea

^c School of Energy and Chemical Engineering, Ulsan National Institute of Science and Technology (UNIST), 50 UNIST-gil, Eonyang-eup, Ulju-gun, Ulsan 44919, Republic of Korea

^d UNIST Central Research Facilities, Ulsan National Institute of Science and Technology (UNIST), 50 UNIST-gil, Eonyang-eup, Ulju-gun, Ulsan 44919, Republic of Korea

^e Department of Chemical and Biological Engineering, Korea University, 145 Anam-ro, Seongbuk-gu, Seoul 02841, Republic of Korea

ARTICLE INFO

Article history:

Received 15 December 2024

Revised 31 January 2025

Accepted 2 February 2025

Available online 20 February 2025

Keywords:

Cationic polymer electrolytes

Weak coordination

Electrode-electrolyte interphase

Fast-charging

Solid-state lithium-metal batteries

ABSTRACT

Despite the growing interest in fast-charging solid-state lithium (Li)-metal batteries (SSLMBs), their practical implementation has yet to be achieved, primarily due to an incomplete understanding of the disparate and often conflicting requirements of the bulk electrolyte and the electrode-electrolyte interphase. Here, we present a weakly coordinating cationic polymer electrolyte (WCPE) specifically designed to regulate the Li⁺ coordination structure, thereby enabling fast-charging SSLMBs. The WCPE comprises an imidazolium-based polycationic matrix combined with a succinonitrile (SN)-based high-concentration electrolyte. Unlike conventional neutral polymer matrices, the polycationic matrix in the WCPE competes with Li⁺ for interactions with SN, weakening the original coordination between SN and Li⁺. This modulation of SN–Li⁺ interaction improves both Li⁺ conductivity of the WCPE ($\sigma_{\text{Li}^+} = 1.29 \text{ mS cm}^{-1}$) and redox kinetics at the electrode-electrolyte interphase. Consequently, SSLMB cells (comprising LiFePO₄ cathodes and Li-metal anodes) with the WCPE achieve fast-charging capability (reaching over 80% state of charge within 10 min), outperforming those of previously reported polymer electrolyte-based SSLMBs.

© 2025 Science Press and Dalian Institute of Chemical Physics, Chinese Academy of Sciences. Published by Elsevier B.V. and Science Press. All rights are reserved, including those for text and data mining, AI training, and similar technologies.

1. Introduction

The growing demand for higher energy density and safer energy storage systems is driving innovation in the battery industry [1–3]. Among emerging technologies, solid-state lithium (Li)-metal batteries (SSLMBs) have garnered considerable attention due to their higher energy density and improved safety characteristics [4–7]. In particular, advancing fast-charging capability has recently emerged as a key focus for expanding the practical applications of SSLMBs [8,9]. However, the fast-charging performance of SSLMBs remains largely underexplored, mainly due to a limited understanding of ion transport phenomena in the bulk electrolyte

and charge transfer at the electrode-electrolyte interphase (EEI) in terms of practical cell application [10–12].

Previous studies on solid-state Li⁺ conductors have predominantly focused on inorganic electrolytes such as sulfides and oxides. Although these inorganic electrolytes exhibit high Li⁺ conductivities comparable to those of liquid electrolytes, their ability to deliver high capacities at elevated current rates is restricted by sluggish redox kinetics at the EEI. Major challenges responsible for the hindered ionic diffusion across this interphase include a limited effective contact area for charge transfer [13,14], the formation of poorly conducting interphases due to chemical and electrochemical instability [15–17], and the presence of space charge layers that alters ion distribution and conductivity near the interface [18–21].

In addition to the aforementioned inorganic electrolytes, polymer-based electrolytes have been investigated for ease of processing, mechanical flexibility, and the ability to form intimate

* Corresponding authors.

E-mail addresses: skkwak@korea.ac.kr (S.K. Kwak), syleek@yonsei.ac.kr (S.-Y. Lee).

¹ These authors contributed equally to this work.

interfacial contact with electrodes [22–24]. Nevertheless, the relatively low ionic conductivities of polymer-based electrolytes have thus far hindered their practical application in SSLMBs [25–27].

Various strategies have been employed to overcome the challenges associated with polymer-based electrolytes. These strategies include the design of new chemical structures [28–30], the incorporation of functional additives [31–33], and the optimization of compositions [34–36]. However, the majority of these efforts have predominantly centered on enhancing Li^+ transport in the bulk electrolyte, often overlooking the critical role of interfacial charge transfer phenomena. To enable fast-charging SSLMBs, it is essential to address the different and often conflicting requirements of both the bulk electrolyte and the EEL. Therefore, a novel approach to polymer-based electrolytes is required based on a mechanistic understanding of bulk ion transport and charge transfer mechanisms.

Here, we present a weakly coordinating cationic polymer electrolyte (WCPE) for fast-charging SSLMBs. The WCPE comprises a 1-allyl-3-methylimidazolium bis(trifluoromethylsulfonyl)imide (AMIM-TFSI)-based polycationic matrix and a succinonitrile (SN)-based high-concentration electrolyte. SN is a representative plastic crystalline organic molecule that acts as a solid solvent capable of dissolving Li salts [37,38]. The WCPE is designed to regulate the Li^+ coordination environment through two key mechanisms described below: static regulation and dynamic regulation (Fig. 1b, c). Static regulation refers to the control of Li^+ coordination in the bulk electrolyte through the formation of a polycation–SN– Li^+ complex, which weakens the original interaction between Li^+ and SN due to competitive binding of SN with the polycation. This reduction in Li^+ coordination facilitates the de-coordination of Li^+ in the bulk electrolyte, thereby improving ion conductivity. Dynamic regulation, on the other hand, occurs at the Li-metal anode, where anions in the Li^+ solvation sheath are repelled during charging [39,40]. This leads to the formation of anion-exclusive Li^+ coordination structures near the anode, which reduces the Li^+ coordination energy, thereby facilitating Li^+ de-coordination and enhancing redox reactions at the EEL. Consequently, the WCPE exhibits high Li^+ conductivity ($\sigma_{\text{Li}^+} = 1.29 \text{ mS cm}^{-1}$) and low charge transfer resistance (R_{ct}) at the EEL.

The electrochemical performance of the WCPE was investigated by incorporating it into a cell (comprising Li-metal anode and LiFePO_4 (LFP) cathode). The WCPE, owing to the aforementioned beneficial effects of its modulated Li^+ coordination, enhances rate performance and cycling retention (86.8% after 250 cycles) of the resulting SSLMBs. Moreover, the WCPE demonstrates superior fast-charging capability, achieving over 80% state of charge (SoC) in less than 10 min, significantly outperforming previously reported SSLMBs with polymer-based electrolytes.

2. Experimental

2.1. Preparation of WCPE

The WCPE and control samples were prepared in an argon (Ar)-filled glove box. AMIM-TFSI ($\geq 98.5\%$, Sigma-Aldrich), 1-allylimidazole ($>97.0\%$, Tokyo Chemical Industry Co., LTD.), and trimethylolpropane propoxylate triacrylate (TPPTA) (Sigma-Aldrich) were purified through the poly(1,1,2,2-tetrafluoroethylene) (PTFE) syringe filter before use. SN ($>98.0\%$, Tokyo Chemical Industry Co., LTD.) was degassed before use according to the procedure described in a reference [41]: (1) bubbling with Ar at 70°C for 45 min, (2) drying under vacuum at 70°C for 15 min, and (3) repeating (1) and (2) three times. Azobisisobutyronitrile (AIBN) (99%, DAEJUNG, Korea) was dried under a vacuum at 20°C for

24 h before use. Lithium bis(fluorosulfonyl)imide (LiFSI) (99.9%, ENCHEM Co., Ltd.) powder was dried under vacuum at 100°C for 24 h before use.

The precursor solution of the WCPE was prepared by mixing AMIM-TFSI, TPPTA, SN, LiFSI, and AIBN in a molar ratio of 8/2/40/12.5/0.1. For Control 2, the precursor solution was prepared by mixing AMIM-TFSI, TPPTA, SN, LiFSI, and AIBN in a molar ratio of 8/2/40/5/0.1. Similarly, the precursor solution for Control 1 was prepared by mixing 1-allylimidazole, TPPTA, SN, LiFSI, and AIBN in a molar ratio of 8/2/40/5/0.1, respectively. To suppress the side reaction of SN with Li-metal, 2 wt% fluoroethylene carbonate (FEC) (99.9%, ENCHEM Co., Ltd.) was added to the precursor solutions [42]. The precursor solutions were stirred vigorously until they became homogeneously transparent. The resulting precursor solutions were injected into CR2032-type coin cell and polymerized in situ at 70°C for 3 h.

2.2. Physicochemical and electrochemical characterization of WCPE

Fourier transform infrared (FT-IR) spectra were collected with a Bruker ALPHA II. Nuclear magnetic resonance (NMR) experiments were performed on a Bruker NEO 600 spectrometer with a 5-mm Prodigy probe. A coaxial sample tube setup was utilized to measure the gel phase of the sample. Specifically, an inner NMR tube (WGS-5BL-SP) containing 220 μL of reference solvent ($\text{DMSO}-d_6$) was inserted into a 5-mm NMR tube (535-PP-7) containing 260 μL of the sample. The ^1H NMR spectra were acquired with zg30 at an operating frequency of 600.25 MHz. The experimental conditions included a pulse length of 11.55 μs , relaxation delay (D_1) of 10 s, and scans (NS) of 16. The ^7Li magic angle spinning (MAS) NMR spectra were obtained utilizing the zg pulse sequence at an operating frequency of 233.28 MHz. The ^7Li longitudinal relaxation times (T_1) were measured utilizing the t1r pulse sequence with a pulse length of 10 μs , D_1 of 20 s, and NS of 16. ^1H - ^1H two-dimensional (2D) nuclear Overhauser effect spectroscopy (NOESY) NMR spectra were acquired utilizing the noesygpph pulse sequence under the following conditions: a pulse length of 11.55 μs and the D_1 of 2 s, NS of 8, 128 increments, and mixing time (D_8) of 700 ms. ^7Li - ^1H 2D heteronuclear Overhauser effect spectroscopy (HOESY) NMR spectra were obtained utilizing hoesy2g pulse duration with a pulse length of 10 μs and D_1 of 5 s, NS of 4, 256 increments, and D_8 of 650 ms. Chemical shifts are referenced to $\text{DMSO}-d_6$ at 2.5 ppm and 1 M LiCl aqueous solution at 0 ppm for ^1H and ^7Li , respectively. Morphological analysis was conducted via field emission scanning electron microscopy (FE-SEM, Hitachi S-4800). Electrochemical impedance spectroscopy (EIS) analysis was performed at a frequency range from 10^{-2} to 10^6 Hz and an applied potential of 10 mV utilizing potentiostats (VMP-300 and VSP, Bio-Logic). The electrochemical stability windows of the electrolytes were evaluated by linear sweep voltammetry (LSV) at a scan rate of 0.1 mV s^{-1} . The Li^+ transference number (t_{Li^+}) was evaluated utilizing a potentiostatic polarization method [43]. The direct current (DC) polarization through a Li^+ non-blocking symmetric cell and its sequential EIS spectra before and after the polarization were analyzed to determine t_{Li^+} .

$$t_{\text{Li}^+} = \frac{I_s(\Delta V - I_0 R_0)}{I_0(\Delta V - I_s R_s)}$$

where ΔV is the applied potential, I_0 and R_0 are the initial current and resistance, and I_s and R_s are the steady-state current and resistance after the polarization, respectively. For the Li-metal cell test, LFP and $\text{LiNi}_{0.7}\text{Co}_{0.1}\text{Mn}_{0.2}\text{O}_2$ (NCM712) cathodes were prepared by casting a slurry mixture (LFP or NCM712/polyvinylidene fluoride/carbon black = 8/1/1, w/w/w) on a carbon-coated aluminum foil

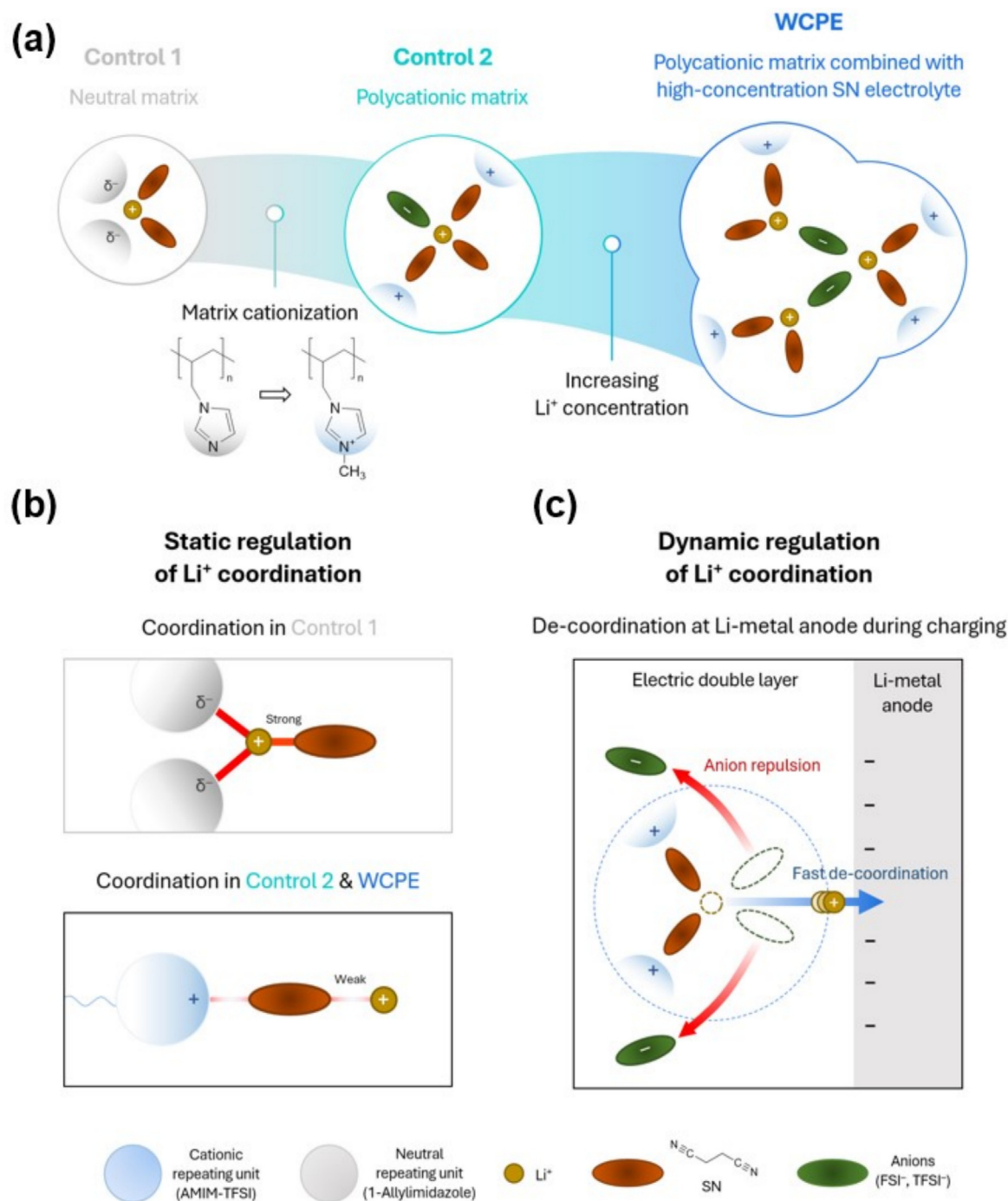


Fig. 1. Design principle of WCPE. (a) Schematic of design procedure and coordination structure of WCPE. (b) Static regulation of Li^+ coordination: Control 1 vs. Control 2 & WCPE. (c) Dynamic regulation of Li^+ coordination: coordination structure near surface of Li-metal anode during charging based on anion repulsion phenomenon.

with a loading of $1\text{--}2 \text{ mg}_{\text{LFP or NCM712}} \text{ cm}^{-2}$. All the cell performance was tested with CR2032 coin-type cells utilizing cycle testers (PNE Solution and McScience).

2.3. MD simulations

Molecular dynamics (MD) simulations were conducted for the WCPE and control samples (i.e., Control 1 and Control 2) to investigate the microscopic solvation structures in the bulk system with the experimental molar ratio. For the simulation, the bulk electrolyte systems with the same ratio as the experimental molar

ratio (i.e., WCPE: AMIM-TFSI/TPPTA/SN/LiFSI = $8/2/40/12.5$, Control 2: AMIM-TFSI/TPPTA/SN/LiFSI = $8/2/40/5$, Control 1: 1-Allylimidazole/TPPTA/SN/LiFSI = $8/2/40/5$) were modeled. The numbers of molecules included in the control samples and the WCPE system for the MD simulations are shown in Table S1. The model systems have a simulation box size of approximately $55 \times 55 \times 55 \text{ (\AA}^3\text{)}$. Initially, all systems were subjected to an NPT (isobaric-isothermal, constant number of particles, pressure, and temperature) ensemble to equilibrate the systems for 5 ns. Subsequently, the equilibrated systems were simulated for 5 ns under the NVT (canonical, constant number of particles, volume, and

temperature) ensemble. All the valence and non-bonded interactions were described by COMPASSIII forcefield [44]. The Nose-Hoover-Langevin thermostat and Berendsen barostat were utilized [45,46]. The coordination number (CN) was defined as $4\pi\rho \int g(r)r^2dr$, where ρ is the average number density, $g(r)$ is the radial distribution function (RDF), and r is the distance from the central atom.

2.4. DFT calculations

Density functional theory (DFT) calculations were performed to determine the Li^+ binding free energy of coordinated structures that were obtained from the last frame of the MD simulation trajectories. The Li^+ binding free energy of each coordinated structure could be calculated with an equation [47].

$$\Delta G_{\text{Li}^+\text{bind}} = \Delta G_{\text{Li}^+\text{CN}} - (m\Delta G_{\text{NM or CM}} + n\Delta G_{\text{SN}} + \Delta G_{\text{Li}^+})$$

where $\Delta G_{\text{Li}^+\text{bind}}$ represents the binding free energy of Li^+ . ΔG_X (i.e., $X = \text{Li}^+\text{CN}$, NM or CM, SN, and Li^+) is the free energy of the Li^+ coordinated structure, neutral moiety or cationic moiety, SN, and Li^+ . In addition, m and n denote the number of neutral or cationic moieties and SN molecules. All DFT calculations were performed with the DMol³ program [48,49]. The B3LYP hybrid functional was utilized for all calculations [50,51]. The spin-polarized calculation was applied with the DNP 4.4 level. All electron relativistic effects were included in the core treatment. The convergence criteria for the self-consistent field were set to 1.0×10^{-6} eV atom⁻¹. The convergence criteria for the geometry optimization were set to 1.0×10^{-5} Ha for energy, 0.002 Ha Å⁻¹ for force, and 0.005 Å for displacement, respectively.

3. Results and discussion

3.1. Design principle of WCPE

The WCPE was synthesized via thermal polymerization of a cationic monomer mixture in the presence of an SN-based high-concentration electrolyte (Fig. S1). The cationic monomer mixture contains AMIM-TFSI as a cationic monomer and TPPTA as a crosslinking agent, with a composition ratio of AMIM-TFSI/TPPTA = 8/2 (mol/mol). The SN-based high-concentration electrolyte consists of 4.3 m LiFSI salt dissolved in SN, where “m” denotes molality (moles of solute per kilogram of solvent). Successful thermal polymerization of the cationic monomer mixture to form a polycationic matrix was confirmed by monitoring the change in FT-IR spectroscopy, specifically the peaks corresponding to C=C bonds (Fig. S2) [52]. For comparative purposes, two control samples were prepared with the same synthetic procedure: Control 1 (comprising an analogous imidazole (i.e., 1-allylimidazole)-based neutral polymer matrix and an SN-based low-concentration electrolyte (1.5 m LiFSI in SN)) and Control 2 (comprising an imidazolium-based polycationic matrix and an SN-based low-concentration electrolyte).

The design principle of the WCPE is conceptually illustrated in Fig. 1(a). The cationic AMIM-TFSI replaces the neutral 1-allylimidazole in Control 1 to create Control 2. This modification allows competition between the polycationic matrix and Li^+ for interactions with SN. Finally, the WCPE was obtained by increasing the concentration of Li salt in the Control 2, effectively increasing the proportion of anions in the Li^+ coordination sheath.

Fig. 1(b) illustrates the static regulation of the Li^+ coordination achieved via cationization of the polymer matrix. This modification leads to the formation of a polycation-SN- Li^+ coordination complex, which weakens the original coordinating interactions between SN and Li^+ due to the competitive interaction of SN with both polycation and Li^+ . Such a reduction in the Li^+ coordination

energy promotes the de-coordination of Li^+ , thereby improving Li^+ migration in the bulk electrolyte [53–56] and electrochemical redox kinetics at the EEI [56–59].

The dynamic regulation of the Li^+ coordination at the Li-metal anode is depicted in Fig. 1(c). During charging, anions in the Li^+ coordination sheath are repelled from the negatively polarized anode [39,40], resulting in anion-exclusive Li^+ coordination structures near the Li-metal anode. As the concentration of Li salt increases, the proportion of anions in the Li^+ solvation sheath grows, further signifying the effect of the anion repulsion at the Li-metal anode. This anion disengagement weakens Li^+ coordination energy at the EEI. Consequently, the WCPE accelerates Li^+ de-coordination and subsequent redox reaction at the Li-metal anode, verified by comparing the R_{ct} values of Li||Li symmetric cells with the WCPE and control samples (Fig. S3).

3.2. Static regulation of Li^+ coordination

The static regulation of the Li^+ coordination by the introduction of the polycation was investigated with 2D ¹H-¹H NOESY and 2D ⁷Li-¹H HOESY NMR spectra, as illustrated in Fig. 2(a, b) and Fig. S4. NOESY and HOESY NMR techniques are known to reveal spatial correlations between species in close proximity (<0.5–1 nm), thereby providing insight into the coordinating interactions between ions and molecules [60,61]. The NOESY and HOESY NMR spectra of the WCPE identified two distinct proton environments originating from the SN: (i) H (from SN at 2.5 ppm [62])–H (from the methyl group of AMIM-TFSI at 3.6 ppm [63]), which indicates proximity between the SN and the imidazolium moiety of the polycation, and (ii) H (from SN)– Li^+ , indicating proximity between SN and Li^+ .

MD simulations were conducted to further elucidate the coordination of SN-polycation. In the WCPE, the presence of the cationic moiety from AMIM-TFSI in the coordination region (~3 Å) of SN was confirmed by the high intensity of the RDF peak and 1 CN with cationic moiety (Fig. S5). This suggests that SN can interact not only with Li^+ but also with polycations. Saturation recovery measurements were conducted to further investigate the molecular dynamics of SN (Fig. S6). The T_1 relaxation times of SN decreased in the presence of the polycation, with values of 1.538 s for Control 1, 1.337 s for Control 2, and 1.097 s for WCPE. This reduction in the T_1 value indicates a decrease in the molecular tumbling rate of SN, which is attributed to the strong coordinating interactions between SN, Li^+ , and the polycation.

In addition, the effect of the introduction of the polycation on the Li^+ coordination strength of SN was investigated. As demonstrated in Fig. S7, the polycation weakens the intermolecular interaction of SN- Li^+ by suppressing electron cloud donation from the nitrile group of SN to Li^+ . The FT-IR spectra of the WCPE displayed an upshift in the characteristic vibrational peak of the coordinating SN bond (from 2276 cm⁻¹ in Control 1 to 2280 cm⁻¹ in the WCPE) [64], indicating an increase in the C≡N bond strength (Fig. 2c). This increased bond strength is attributed to a more localized electron cloud around the nitrile group. The electron localization in the nitrile group was further investigated via ¹⁵N MAS NMR spectroscopy (Fig. 2d). As the proportion of coordination of polycation-SN- Li^+ increases in the sequence of Control 1, Control 2, and WCPE, a gradual shielding of the N (nitrogen) nuclei in the C≡N bond was observed [65], exhibiting the viable role of the incorporated polycation.

To further investigate the effect of the polycation on the Li^+ coordination ability of SN in the WCPE, ⁷Li MAS NMR spectroscopy was performed (Fig. 2e). Compared to Control 1, the Li^+ peak in Control 2 shifted upfield, disclosing the formation of an anion-rich Li^+ coordination sheath as a result of the weakened Li^+ coordination of SN [66,67]. The most pronounced upfield shift of the Li^+

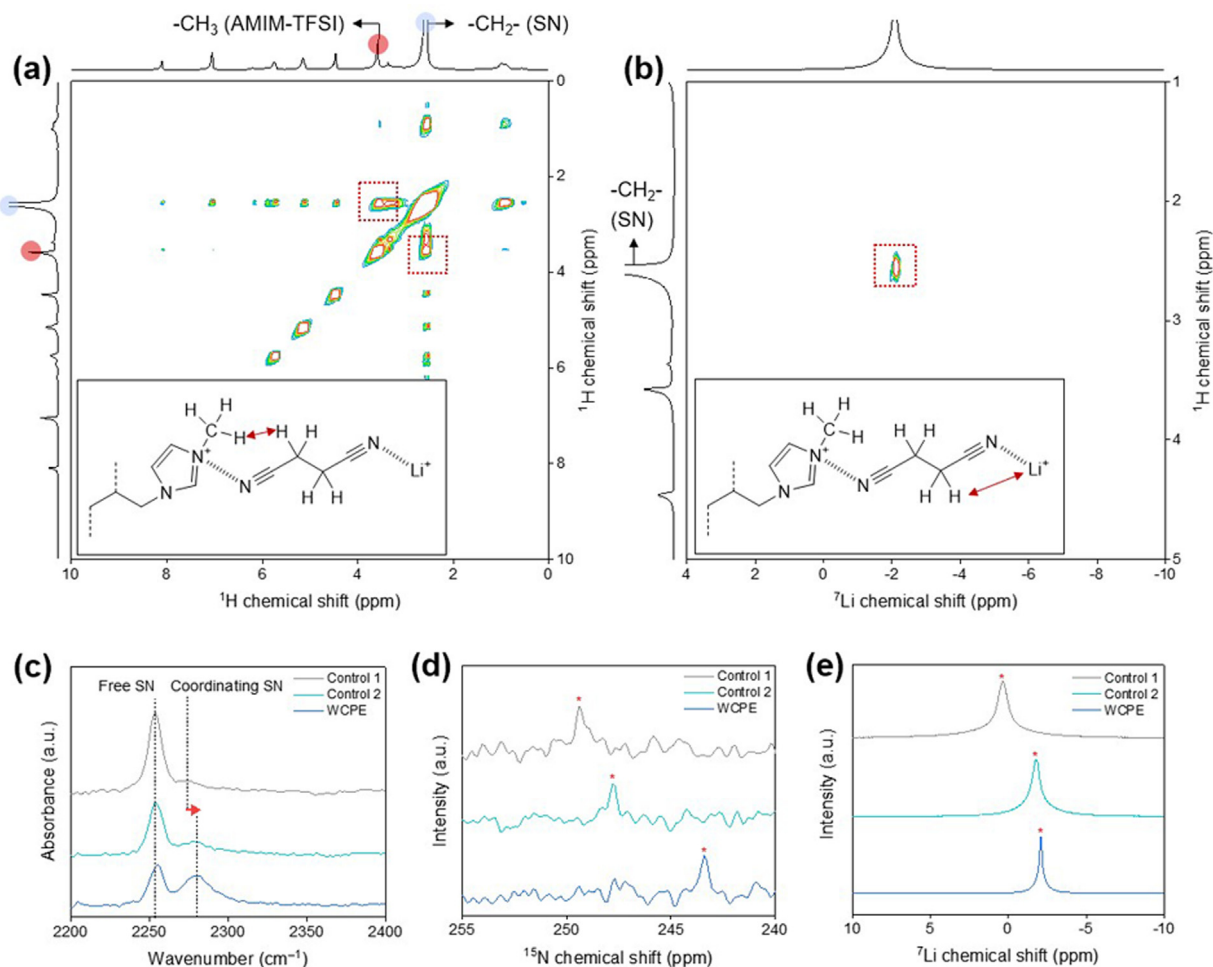


Fig. 2. Static regulation of Li^+ coordination. (a) 2D ^1H - ^1H NOESY NMR spectra and (b) 2D ^7Li - ^1H HOESY NMR spectra of WCPE. The insets show the specific interactions corresponding to each peak. (c) FT-IR spectra (focusing on C–N stretching peaks of SN) and (d) ^{15}N MAS NMR spectra (focusing on nitrile peaks of SN) of WCPE (vs. control samples). (e) ^7Li MAS NMR spectra of WCPE (vs. control samples).

peak was observed in the WCPE, reflecting strong Li^+ -anion pairing due to the combined effect of the high-concentration electrolyte and the coordination of polycation-SN- Li^+ .

3.3. Dynamic regulation of Li^+ coordination

The dynamic regulation of the Li^+ coordination structure, focusing on the anion repulsion on the surface of Li-metal anodes during charging, was analyzed with the Gouy-Chapman-Stern model. In this model, the thickness of the electric double layer (EDL) is the sum of the Stern layer and the diffusion layer [68]. Given the higher proportion of anions in the Li^+ coordination sheath than that in the control samples, the WCPE may exhibit the most significant shrinkage in Li^+ coordination radius at the EDL due to the anion repulsion. Hence, the EDL between the WCPE and the Li-metal anode could be densely packed with Li^+ , leading to the smallest EDL thickness (Fig. 3a, b).

To quantify the EDL thickness, the EDL capacitance (C_{EDL}) was measured for the WCPE and control samples utilizing cyclic voltammetry (CV) at various scan rates (Fig. S8) [69]. C_{EDL} is estimated by an equation $C_{\text{EDL}} = \frac{\varepsilon A}{d}$, where ε is the dielectric constant of the electrolytes, A is the surface area of the electrodes, and d is the EDL thickness. The WCPE and control samples contain SN as a main component and the experiment was conducted using Li-metal anodes of fixed dimensions. Consequently, the ε and A were

assumed to be equivalent for all samples. Under these conditions, the highest C_{EDL} (1.09 mF cm^{-2}) was observed for the WCPE (Fig. 3c), indicating the smallest d . This result is consistent with the anion repulsion phenomenon at the EEI.

Based on the understanding of the Li^+ coordination structure obtained from the MD simulations, DFT calculations were performed to further verify the viability of the dynamic regulation of the coordination structure. Prior to conducting the DFT calculations, the Li^+ coordination structure in the WCPE was analyzed using the RDF and CN analyses (Fig. S9). The CN for Li^+ -anions in the WCPE increased to 3, with this interaction predominating within the defined interaction region of approximately 2.5 Å. As discussed in the previous EDL analysis, the negative polarization of the Li-metal anode induces anion repulsion from the anode surface [39,40]. Therefore, the $\Delta G_{\text{Li}^+ \text{ bind}}$ for the coordination structures was calculated using the MD simulation results (Fig. 3d), in which the effects of anions were excluded based on the anion repulsion. The WCPE exhibited the lowest $\Delta G_{\text{Li}^+ \text{ bind}}$, indicating the weakest Li^+ coordination strength at the EEI.

3.4. Electrochemical compatibility between WCPE and Li-metal anode

To demonstrate the beneficial effect of the WCPE strategy, which allows the static and dynamic regulation of Li^+ coordination,

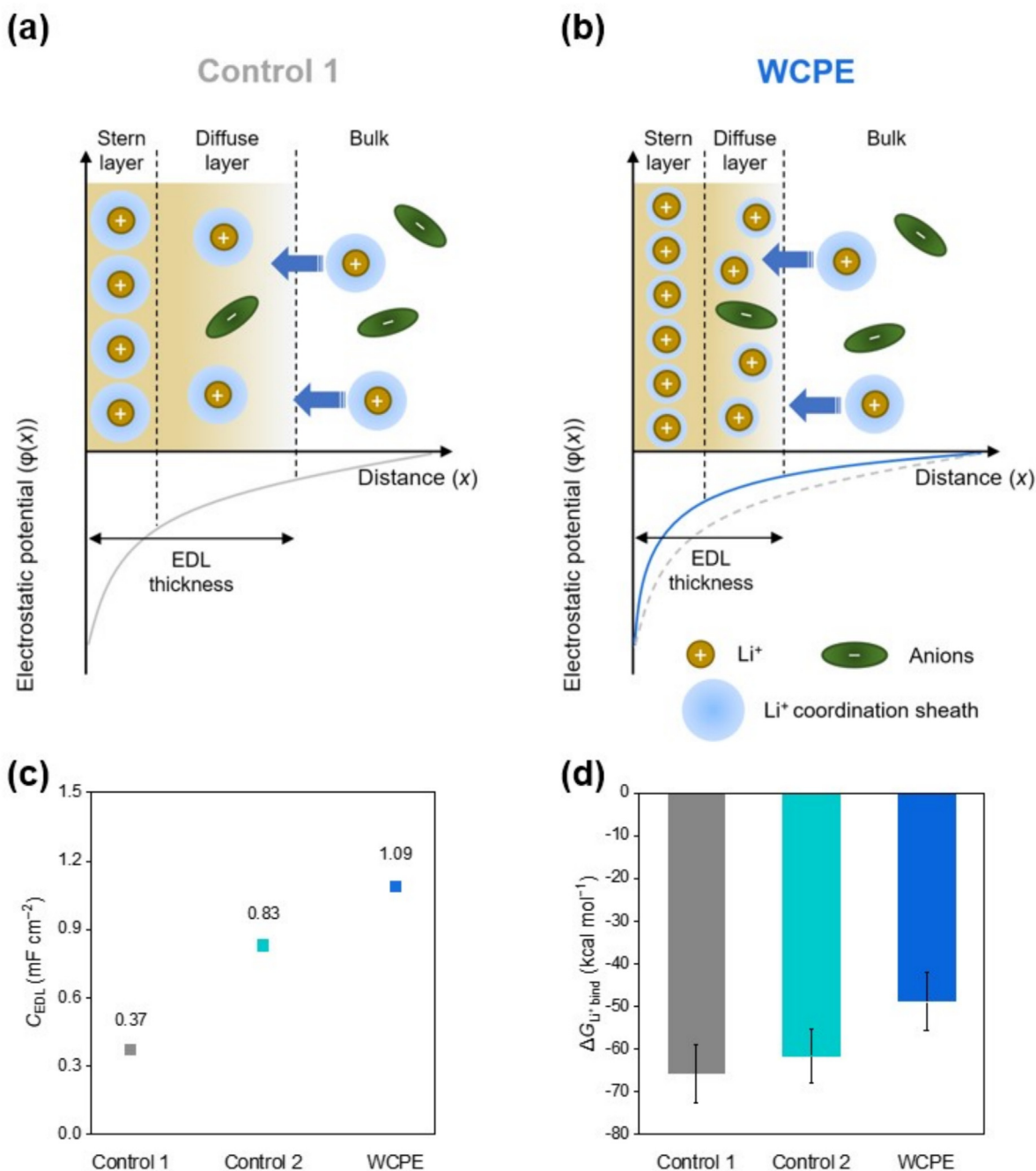


Fig. 3. Dynamic regulation of Li^+ coordination. Schematic of anion repulsion on the surface of Li-metal anode during charging based on Gouy-Chapman-Stern model of (a) Control 1 and (b) WCPE. Li^+ and anions are exclusively depicted. (c) C_{EDL} between Li-metal anode and WCPE (vs. control samples). (d) $\Delta G_{\text{Li}^+ \text{ bind}}$ for coordinated structures of WCPE (vs. control samples).

on the redox kinetics at the EEI, the R_{ct} values of $\text{Li}||\text{Li}$ symmetric cells with the WCPE and control samples were examined via EIS at 25 °C (Fig. 4a and Fig. S10). The WCPE had a significantly lower R_{ct} value ($126 \Omega \text{ cm}^2$) compared to the control samples, exhibiting the effectiveness of the coordination structure regulation. This improvement in the R_{ct} of the WCPE was observed over a wide temperature range (Fig. S11). In addition, the Tafel plots of the control samples revealed lower exchange current densities of 0.06 mA cm^{-2} (Control 1) and 0.38 mA cm^{-2} (Control 2), respectively (Fig. 4b), indicating sluggish Li^+ de-coordination kinetics. In contrast, the WCPE displayed a higher exchange current density of 0.60 mA cm^{-2} . These results demonstrate that the WCPE accelerates the electrochemical reaction kinetics via the efficient Li^+

de-coordination, highlighting its potential as a promising polymer-based electrolyte for fast-charging SSLMBs.

The ion transport phenomena of the WCPE were investigated in detail, revealing the crucial role of the polycationic matrix in facilitating Li^+ transport. The Li^+ conductivity (σ_{Li^+} = ionic conductivity (σ) \times cationic transference number (t_{Li^+})) more than doubled from 0.60 mS cm^{-1} for Control 1 to 1.25 mS cm^{-1} for Control 2 at 25 °C (Fig. 4c, Figs. S12, S13 and Tables S2, S3). Furthermore, the WCPE had a higher σ_{Li^+} of 1.29 mS cm^{-1} at 25 °C. This beneficial effect was further verified by conducting the saturation recovery measurement [70] based on the ^7Li MAS NMR analysis (Fig. 4c and Fig. S14). Both the WCPE and Control 2 exhibited larger T_1 values (1.021 s for WCPE and 1.020 s for Control 2) compared to Control

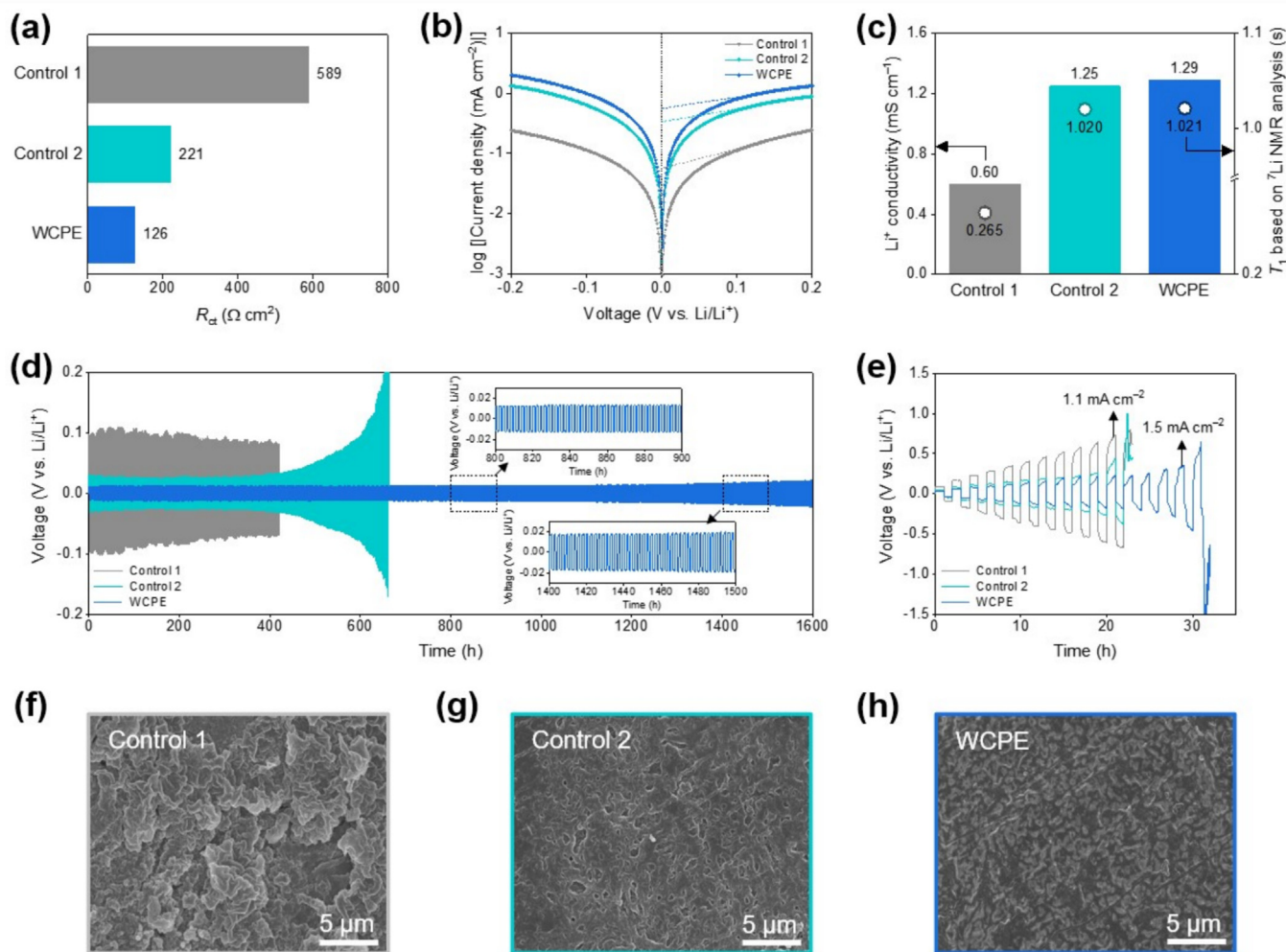


Fig. 4. Electrochemical compatibility between WCPE and Li-metal anode. (a) R_{ct} of Li||Li symmetric cells with WCPE (vs. control samples) at 25 °C. (b) Tafel plots of Li||Li symmetric cells with WCPE (vs. control samples) at 25 °C. (c) Li^+ conductivity (σ_{Li^+}) and T_1 of WCPE (vs. control samples) at 25 °C. (d) Voltage profiles of Li||Li symmetric cells with WCPE (vs. control samples) at a current density of 0.1 mA cm^{-2} and capacity of 0.1 mAh cm^{-2} . (e) Voltage profiles of Li||Li symmetric cells with WCPE (vs. control samples) as a function of current density, in which applied current density was increased from 0.1 to 1.5 mA cm^{-2} with a step increase of 0.1 $\text{mA cm}^{-2} \text{ h}^{-1}$. SEM images (surface view) of cycled Li-metal anodes with (f) Control 1, (g) Control 2, and (h) WCPE.

1 (0.265 s), indicating the faster Li^+ mobility enabled by the presence of polycations.

These advantageous effects of the WCPE on the redox kinetics and σ_{Li^+} enhanced the Li plating/stripping behavior of the Li||Li symmetric cell (Fig. 4d). Notably, the WCPE demonstrated stable Li plating/stripping cyclability for 1600 h, outperforming the control samples. Moreover, the WCPE exhibited a higher critical current density (CCD) of 1.5 mA cm^{-2} compared to the control samples (Fig. 4e). These effects were further corroborated by analyzing the structural change of Li-metal electrodes after the cycling test (Fig. 4f–h). A dense and uniform surface morphology was observed on the cycled Li-metal electrode (after 50 cycles) assembled with the WCPE. In contrast, the Li-metal electrodes assembled with the control samples exhibited random and needle-like Li dendrites. This comparative analysis confirms the electrochemical viability of the WCPE in promoting redox homogeneity on the surface of Li-metal electrodes.

3.5. Electrochemical performance of SSLMBs with WCPE

The effect of Li^+ coordination regulation on the electrochemical performance of the WCPE was investigated with SSLMB cells

(Li-metal anode||LFP cathode). The WCPE and control samples exhibited a stable electrochemical stability window above 4.0 V vs. Li/Li^+ (Fig. S15). The cycling performance was examined at a charge/discharge current density of 1.0/1.0 C at 25 °C (Fig. 5a). The WCPE cell exhibited superior capacity retention (86.8% after 250 cycles) compared to the control cells. Furthermore, the WCPE cell demonstrated reduced average discharge voltage decay (Fig. 5b) and lower cell voltage hysteresis (Fig. S16) compared to the control cells, exhibiting improved Li^+ transport and redox kinetics due to the low de-coordination barrier of the WCPE. In addition, the WCPE cell achieved higher discharge rate capability over a wide range of discharge current densities (0.1–4.0 C) (Fig. 5c). Meanwhile, electrochemical performance of the WCPE in a Li||NCM712 cell was investigated at 25 °C under a charge/discharge current density of 1.0/1.0 C. The cell maintained a specific discharge capacity of 166.4 $\text{mAh g}_{\text{NCM712}}^{-1}$ over 40 cycles (Fig. S17), demonstrating the potential applicability of the WCPE in high-voltage systems.

Fast de-coordination kinetics and efficient Li^+ transport in electrolytes are essential to enable fast-charging SSLMBs. To investigate the electrochemical performance under challenging conditions, the cycling behavior of the SSLMB cell was evaluated

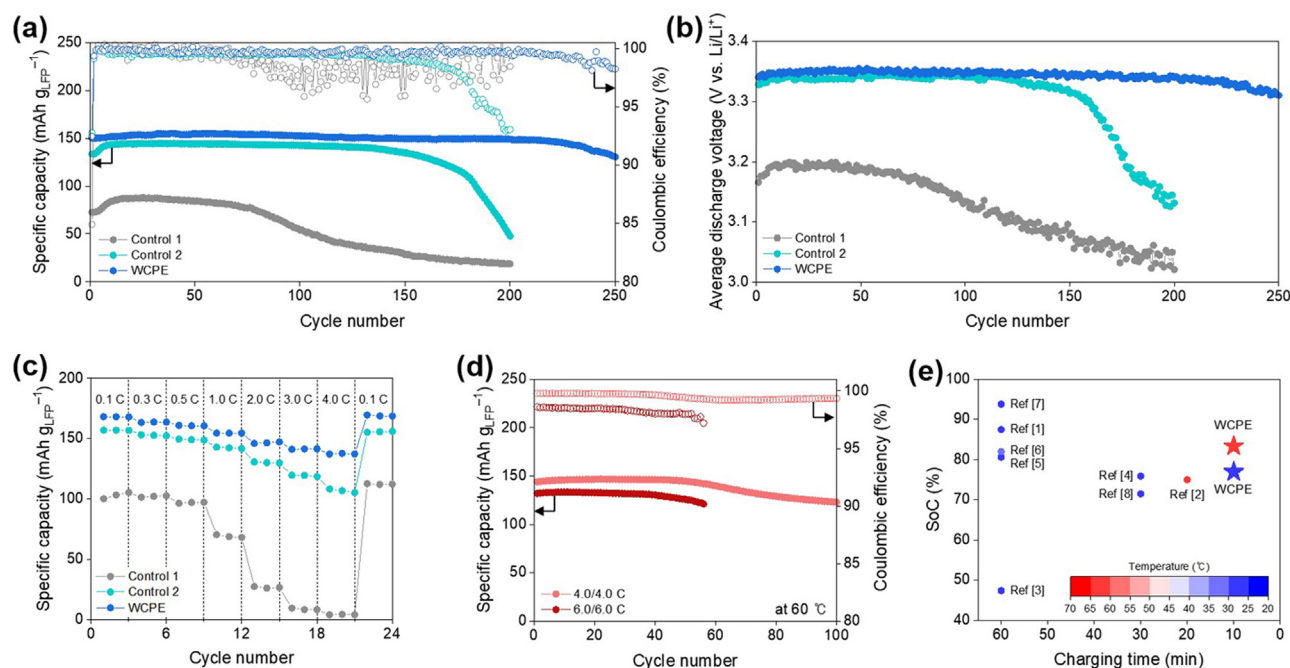


Fig. 5. Electrochemical performance of SSLMBs with WCPE. (a) Cycling performance and (b) average discharge voltage of Li||LFP cells with WCPE (vs. control samples) at charge/discharge current density of 1.0/1.0 C under voltage range of 2.5–4.0 V at 25 °C. (c) Rate performance of Li||LFP cells with WCPE (vs. control samples), in which the discharge current density varied from 0.1 to 4.0 C at fixed charge current density of 0.1 C. (d) Cycling performance of Li||LFP cells with WCPE at charge/discharge current densities of 4.0/4.0 C and 6.0/6.0 C under voltage range of 2.5–4.0 V at 60 °C. (e) Comparison between WCPE cell and previously reported SSLMBs containing polymer-based electrolytes in terms of charging time (x-axis), SoC (y-axis), and operating temperature (heatmap). Details on the references are provided in Table S4.

at high current densities (4.0 and 6.0 C) and an elevated operating temperature of 60 °C (Fig. 5d). The temperature of 60 °C was deliberately chosen as a harsh condition to promote ion (Fe²⁺) dissolution from the LFP cathode [71,72]. Under these constrained operating conditions, the SSLMB cells with the WCPE exhibited high specific discharge capacities (146.8 and 133.4 mAh g_{LFP}⁻¹ at 4.0 and 6.0 C, respectively) with stable cycle retention, outperforming the control cells (Fig. S18). Furthermore, the high-rate capability of SSLMB cells with the WCPE was evaluated at 25 °C (Fig. S19). Even at 6.0 C, the WCPE cell maintained a high specific discharge capacity of 123.2 mAh g_{LFP}⁻¹ with stable cycle retention, demonstrating its effectiveness in facilitating fast Li⁺ transport and enhancing redox kinetics.

To further underscore such an exceptional fast-charging capability of the WCPE cell, its SoC and charging time (83.4% within 10 min at 60 °C and 77.0% within 10 min at 25 °C) were compared with those of previously reported SSLMBs containing polymer-based electrolytes free of volatile solvents (Fig. 5e and Table S4). This comparative analysis demonstrates the WCPE as a promising solid-state electrolyte design, representing a significant advancement in the pursuit of fast-charging SSLMBs.

4. Conclusions

In summary, we have demonstrated the potential viability of the WCPE as a class of solid-state electrolytes for fast-charging SSLMBs. The WCPE facilitated both static and dynamic modulation of the Li⁺ coordination structure, contributing to enhanced ion transport and redox kinetics. The static regulation was achieved through ion-dipole interactions between the polycationic matrix and SN, thereby weakening Li⁺ coordination strength in ion clusters within the bulk electrolyte. This mechanism effectively reduced the Li⁺ de-coordination energy, leading to high σ_{Li} (1.29 mS cm⁻¹). The dynamic regulation occurred at the EEI, where

anion repulsion within the Li⁺ coordination sheath further lowered Li⁺ de-coordination barrier, facilitating electrochemical reaction kinetics. Benefiting from these advantageous effects, the WCPE enabled the SSLMB (Li-metal anode||LFP cathode) to exhibit improved rate performance and cycling stability (86.8% after 250 cycles). Notably, the WCPE provided exceptional fast-charging capability (reaching 83.4% SoC within 10 min), far surpassing those of previously reported SSLMBs based on conventional polymer-based electrolytes. The WCPE strategy, based on the regulation of the Li⁺ coordination chemistry, is a viable solid-state electrolyte platform to address the pressing challenge of fast-charging SSLMBs, which has remained unsolved with the prevalent inorganic solid electrolytes.

CRedit authorship contribution statement

Soohyoung Lee: Writing – original draft, Visualization, Validation, Methodology, Investigation, Formal analysis, Data curation, Conceptualization. **Kyeong-Seok Oh:** Writing – original draft, Visualization, Validation, Methodology, Investigation, Formal analysis, Data curation, Conceptualization. **Ji Eun Lee:** Writing – original draft, Visualization, Validation, Methodology, Formal analysis. **Sun-Phil Han:** Methodology, Formal analysis. **Hong-I Kim:** Methodology, Investigation, Conceptualization. **Sang Kyu Kwak:** Writing – review & editing, Supervision, Resources, Funding acquisition. **Sang-Young Lee:** Writing – review & editing, Supervision, Resources, Funding acquisition.

Declaration of competing interest

The authors declare that they have no known competing financial interests or personal relationships that could have appeared to influence the work reported in this paper.

Acknowledgments

This work was supported by the Basic Science Research Program (RS-2024-00344021, RS-2023-00261543, and RS-2023-00257666) through the National Research Foundation of Korea (NRF), the National Research Council of Science 000), and Korea Institute for Advancement of Technology (KIAT) grant funded by the Korea Government (MOTIE) (RS-2024-00420590, HRD Program for Industrial Innovation). The computational resources were provided by KITSI (KSC-2024-CRE-0143).

Appendix A. Supplementary material

Supplementary material to this article can be found online at <https://doi.org/10.1016/j.jechem.2025.02.002>.

References

- [1] M. Armand, J.-M. Tarascon, *Nature* 451 (2008) 652–657.
- [2] R. Schmich, R. Wagner, G. Hörpel, T. Placke, M. Winter, *Nat. Energy* 3 (2018) 267–278.
- [3] X.-Q. Xu, X.-B. Cheng, F.-N. Jiang, S.-J. Yang, D. Ren, P. Shi, H. Hsu, H. Yuan, J.-Q. Huang, M. Ouyang, Q. Zhang, *SusMat* 2 (2022) 435–444.
- [4] J.C. Bachman, S. Muy, A. Grimaud, H.-H. Chang, N. Pour, S.F. Lux, O. Paschos, F. Maglia, S. Lupart, P. Lamp, L. Giordano, Y. Shao-Horn, *Chem. Rev.* 116 (2016) 140–162.
- [5] M. Winter, B. Barnett, K. Xu, *Chem. Rev.* 118 (2018) 11433–11456.
- [6] A. Banerjee, X. Wang, C. Fang, E.A. Wu, Y.S. Meng, *Chem. Rev.* 120 (2020) 6878–6933.
- [7] P. Xu, Z.-Y. Shuang, C.-Z. Zhao, X. Li, L.-Z. Fan, A. Chen, H. Chen, E. Kuzmina, E. Karaseva, V. Kolosnitsyn, X. Zeng, P. Dong, Y. Zhang, M. Wang, Q. Zhang, *Sci. China Chem.* 67 (2024) 67–86.
- [8] Y. Liu, Y. Zhu, Y. Cui, *Nat. Energy* 4 (2019) 540–550.
- [9] X.-G. Yang, G. Zhang, S. Ge, C.-Y. Wang, *Proc. Natl. Acad. Sci. U.S.A.* 115 (2018) 7266–7271.
- [10] J. Janek, W.G. Zeier, *Nat. Energy* 1 (2016) 1–4.
- [11] J. Janek, W.G. Zeier, *Nat. Energy* 8 (2023) 230–240.
- [12] E.R. Logan, J.R. Dahm, *Trends Chem.* 2 (2020) 354–366.
- [13] K.H. Park, Q. Bai, D.H. Kim, D.Y. Oh, Y. Zhu, Y. Mo, Y.S. Jung, *Adv. Energy Mater.* 8 (2018) 1800035.
- [14] K.J. Kim, M. Balaish, M. Wadaguchi, L. Kong, J.L.M. Rupp, *Adv. Energy Mater.* 11 (2021) 2002689.
- [15] P. Hartmann, T. Leichtweiss, M.R. Busche, M. Schneider, M. Reich, J. Sann, P. Adelhelm, J. Janek, *J. Phys. Chem. C* 117 (2013) 21064–21074.
- [16] T. Krauskopf, F.H. Richter, W.G. Zeier, J. Janek, *Chem. Rev.* 120 (2020) 7745–7794.
- [17] S. Kim, J.-S. Kim, L. Miara, Y. Wang, S.-K. Jung, S.Y. Park, Z. Song, H. Kim, M. Badding, J. Chang, V. Roveg, G. Yoon, R. Kim, J.-H. Kim, K. Yoon, D. Im, K. Kang, *Nat. Commun.* 13 (2022) 1883.
- [18] T. Famprikis, P. Canepa, J.A. Dawson, M.S. Islam, C. Masquelier, *Nat. Mater.* 18 (2019) 1278–1291.
- [19] Z. Cheng, M. Liu, S. Ganapathy, C. Li, Z. Li, X. Zhang, P. He, H. Zhou, M. Wagemaker, *Joule* 4 (2020) 1311–1323.
- [20] L. Wang, R. Xie, B. Chen, X. Yu, J. Ma, C. Li, Z. Hu, X. Sun, C. Xu, S. Dong, T.-S. Chan, J. Luo, G. Cui, L. Chen, *Nat. Commun.* 11 (2020) 5889.
- [21] Z. Gu, J. Ma, F. Zhu, T. Liu, K. Wang, C.-W. Nan, Z. Li, C. Ma, *Nat. Commun.* 14 (2023) 1632.
- [22] D. Zhou, D. Shanmukaraj, A. Tkacheva, M. Armand, G. Wang, *Chem* 5 (2019) 2326–2352.
- [23] X. Lu, Y. Wang, X. Xu, B. Yan, T. Wu, L. Lu, *Adv. Energy Mater.* 13 (2023) 2301746.
- [24] Z. Jia, Y. Liu, H. Li, Y. Xiong, Y. Miao, Z. Liu, F. Ren, *J. Energy Chem.* 92 (2024) 548–571.
- [25] Z. Li, J. Fu, X. Zhou, S. Gui, L. Wei, H. Yang, H. Li, X. Guo, *Adv. Sci.* 10 (2023) 2201718.
- [26] Z. Song, F. Chen, M. Martinez-Ibañez, W. Feng, M. Forsyth, Z. Zhou, M. Armand, H. Zhang, *Nat. Commun.* 14 (2023) 4884.
- [27] N.J. Shah, C. Fang, N.C. Osti, E. Mamontov, X. Yu, J. Lee, H. Watanabe, R. Wang, N.P. Balsara, *Nat. Mater.* 23 (2024) 664–669.
- [28] C. Wang, H. Liu, Y. Liang, D. Li, X. Zhao, J. Chen, W. Huang, L. Gao, L.-Z. Fan, *Adv. Funct. Mater.* 33 (2023) 2209828.
- [29] S. Han, P. Wen, H. Wang, Y. Zhou, Y. Gu, L. Zhang, Y. Shao-Horn, X. Lin, M. Chen, *Nat. Mater.* 22 (2023) 1515–1522.
- [30] K. Guo, S. Li, J. Wang, Z. Shi, Y. Wang, Z. Xue, *ACS Energy Lett.* 9 (2024) 843–852.
- [31] W. Liu, S.W. Lee, D. Lin, F. Shi, S. Wang, A.D. Sendek, Y. Cui, *Nat. Energy* 2 (2017) 17035.
- [32] Y. Fu, K. Yang, S. Xue, W. Li, S. Chen, Y. Song, Z. Song, W. Zhao, Y. Zhao, F. Pan, L. Yang, X. Sun, *Adv. Funct. Mater.* 33 (2023) 2210845.
- [33] X. Yu, L. Zhao, Y. Li, Y. Jin, D.J. Politis, H. Liu, H. Wang, M. Liu, Y.-B. He, L. Wang, *ACS Energy Lett.* 9 (2024) 2109–2115.
- [34] X. Wang, F. Chen, G.M.A. Girard, H. Zhu, D.R. MacFarlane, D. Mecerreyes, M. Armand, P.C. Howlett, M. Forsyth, *Joule* 3 (2019) 2687–2702.
- [35] F. Chen, X. Wang, M. Armand, M. Forsyth, *Nat. Mater.* 21 (2022) 1175–1182.
- [36] S.D. Jones, H. Nguyen, P.M. Richardson, Y.-Q. Chen, K.E. Wyckoff, C.J. Hawker, R. J. Clément, G.H. Fredrickson, R.A. Segalman, *ACS Cent. Sci.* 8 (2022) 169–175.
- [37] H.-J. Ha, E.-H. Kil, Y.H. Kwon, J.Y. Kim, C.K. Lee, S.-Y. Lee, *Energy Environ. Sci.* 5 (2012) 6491–6499.
- [38] K.-H. Choi, S.-J. Cho, S.-H. Kim, Y.H. Kwon, J.Y. Kim, S.-Y. Lee, *Adv. Funct. Mater.* 24 (2014) 44–52.
- [39] X. Fan, X. Ji, L. Chen, J. Chen, T. Deng, F. Han, J. Yue, N. Piao, R. Wang, X. Zhou, X. Xiao, L. Chen, C. Wang, *Nat. Energy* 4 (2019) 882–890.
- [40] J. Holoubek, H. Liu, Z. Wu, Y. Yin, X. Xing, G. Cai, S. Yu, H. Zhou, T.A. Pascal, Z. Chen, P. Liu, *Nat. Energy* 6 (2021) 303–313.
- [41] J. Han, M.J. Lee, K. Lee, Y.J. Lee, S.H. Kwon, J.H. Min, E. Lee, W. Lee, S.W. Lee, B.J. Kim, *Adv. Mater.* 35 (2023) 2205194.
- [42] C. Fu, Y. Ma, S. Lou, C. Cui, L. Xiang, W. Zhao, P. Zuo, J. Wang, Y. Gao, G. Yin, J. Mater. Chem. A 8 (2020) 2066–2073.
- [43] J. Evans, C.A. Vincent, P.G. Bruce, *Polymer* 28 (1987) 2324–2328.
- [44] R.L.C. Akkermans, N.A. Spenley, S.H. Robertson, *Mol. Simul.* 47 (2021) 540–551.
- [45] A.A. Samoletov, C.P. Dettmann, M.A.J. Chaplain, *J. Stat. Phys.* 128 (2007) 1321–1336.
- [46] H.J.C. Berendsen, J.P.M. Postma, W.F. van Gunsteren, A. DiNola, J.R. Haak, *J. Chem. Phys.* 81 (1984) 3684–3690.
- [47] W. Cui, Y. Lansac, H. Lee, S.-T. Hong, Y.H. Jang, *Phys. Chem. Chem. Phys.* 18 (2016) 23607–23612.
- [48] B. Delley, *J. Chem. Phys.* 92 (1990) 508–517.
- [49] B. Delley, *J. Chem. Phys.* 113 (2000) 7756–7764.
- [50] A.D. Becke, *J. Chem. Phys.* 98 (1993) 5648–5652.
- [51] P.J. Stephens, F.J. Devlin, C.F. Chabalowski, M.J. Frisch, *J. Phys. Chem.* 98 (1994) 11623–11627.
- [52] K.-S. Oh, J.-H. Kim, S.-H. Kim, D. Oh, S.-P. Han, K. Jung, Z. Wang, L. Shi, Y. Su, T. Yim, S. Yuan, S.-Y. Lee, *Adv. Energy Mater.* 11 (2021) 2101813.
- [53] D.G. Mackanic, W. Michaels, M. Lee, D. Feng, J. Lopez, J. Qin, Y. Cui, Z. Bao, *Adv. Energy Mater.* 8 (2018) 1800703.
- [54] Z. Tian, L. Hou, D. Feng, Y. Jiao, P. Wu, *ACS Nano* 17 (2023) 3786–3796.
- [55] H. Peng, T. Long, J. Peng, H. Chen, L. Ji, H. Sun, L. Huang, S.-G. Sun, *Adv. Energy Mater.* 14 (2024) 2400428.
- [56] P. Xu, Y.-C. Gao, Y.-X. Huang, Z.-Y. Shuang, W.-J. Kong, X.-Y. Huang, W.-Z. Huang, N. Yao, X. Chen, H. Yuan, C.-Z. Zhao, J.-Q. Huang, Q. Zhang, *Adv. Mater.* 36 (2024) 2409489.
- [57] Y. Chen, Q. He, Y. Zhao, W. Zhou, P. Xiao, P. Gao, N. Tavajohi, J. Tu, B. Li, X. He, L. Xing, X. Fan, J. Liu, *Nat. Commun.* 14 (2023) 8326.
- [58] X. Cao, W. Xu, D. Zheng, F. Wang, Y. Wang, X. Shi, X. Lu, *Angew. Chem. Int. Ed.* 63 (2024) e202317302.
- [59] H. Zhang, Z. Zeng, Q. Wu, X. Wang, M. Qin, S. Lei, S. Cheng, J. Xie, *J. Energy Chem.* 90 (2024) 380–387.
- [60] S. Khatun, E.W. Castner Jr., *J. Phys. Chem. B* 119 (2015) 9225–9235.
- [61] V. Kumar, R.R. Reddy, B.V.N.P. Kumar, C.V. Avadhani, S. Ganapathy, N. Chandrakumar, S. Sivaram, *J. Phys. Chem. C* 123 (2019) 9661–9672.
- [62] D. Reber, O. Borodin, M. Becker, D. Rentsch, J.H. Thienenkamp, R. Grissa, W. Zhao, A. Aribia, G. Brunklaus, C. Battaglia, R.-S. Kühnel, *Adv. Funct. Mater.* 32 (2022) 2112138.
- [63] C. D'Agostino, M.D. Mantle, C.L. Mullan, C. Hardacre, L.F. Gladden, *ChemPhysChem* 19 (2018) 1081–1088.
- [64] Y. Shen, G.-H. Deng, C. Ge, Y. Tian, G. Wu, X. Yang, J. Zheng, K. Yuan, *Phys. Chem. Chem. Phys.* 18 (2016) 14867–14873.
- [65] E.F. Mooney, P.H. Winson, *Annu. Rep. NMR Spectrosc.* 2 (1969) 125–152.
- [66] Z. Yu, P.E. Rudnicki, Z. Zhang, Z. Huang, H. Celik, S.T. Oyakhire, Y. Chen, X. Kong, S.C. Kim, X. Xiao, H. Wang, Y. Zheng, G.A. Kamat, M.S. Kim, S.F. Bent, J. Qin, Y. Cui, Z. Bao, *Nat. Energy* 7 (2022) 94–106.
- [67] Q. Wang, Y. Ma, X. Jia, D. Zhang, Z. Li, H. Sun, Q. Sun, B. Wang, L.-Z. Fan, *J. Energy Chem.* 96 (2024) 633–641.
- [68] X. Shi, J. Xie, F. Yang, F. Wang, D. Zheng, X. Cao, Y. Yu, Q. Liu, X. Lu, *Angew. Chem. Int. Ed.* 61 (2022) e202214773.
- [69] G. Li, Z. Zhao, S. Zhang, L. Sun, M. Li, J.A. Yuwono, J. Mao, J. Hao, J. Vongsvivut, L. Xing, C.-X. Zhao, Z. Guo, *Nat. Commun.* 14 (2023) 6526.
- [70] K. Jeong, S. Park, G.Y. Jung, S.H. Kim, Y.-H. Lee, S.K. Kwak, S.-Y. Lee, *J. Am. Chem. Soc.* 141 (2019) 5880–5885.
- [71] Z. Zhang, T. Zeng, H. Lu, M. Jia, J. Li, Y. Lai, *ECS Electrochem. Lett.* 1 (2012) A74–A76.
- [72] S. Tang, Y. Liang, Y. Peng, Y. Hu, Y. Liao, X. Yang, H. Zhang, Y. Lin, K. Zhang, J. Liang, B. Li, G. Zhao, Y. Wei, Z. Gong, Y. Yang, *Adv. Energy Mater.* 15 (2025) 2402842.